Experimental observation of current-driven antiskyrmion sliding in stripe domains

Zhidong He[1,2], Zhuolin Li[1,2], Zhaohui Chen[3], Zhan Wang[1], Jun Shen[4], Shouguo Wang[5], Cheng Song [6], Tongyun Zhao[1,2], Jianwang Cai [1,2], Shi-Zeng Lin [7]✉, Ying Zhang [1,2,8]✉ & Baogen Shen[1,2,9]

Magnetic skyrmions are promising as next-generation information units. Their antiparticle—the antiskyrmion—has also been discovered in chiral magnets. Here we experimentally demonstrate antiskyrmion sliding in response to a pulsed electric current at room temperature without the requirement of an external magnetic field. This is realized by embedding antiskyrmions in helical stripe domains, which naturally provide one-dimensional straight tracks along which antiskyrmion sliding can be easily launched with low current density and without transverse deflection from the antiskyrmion Hall effect. The higher mobility of the antiskyrmions in the background of helical stripes in contrast to the typical ferromagnetic state is a result of intrinsic material parameters and elastic energy of the stripe domain, thereby smearing out the random pinning potential, as supported by micromagnetic simulations. The demonstration and comprehensive understanding of antiskyrmion movement along naturally straight tracks offers a new perspective for (anti)skyrmion application in spintronics.

Magnetic topological spin textures such as skyrmions and antiskyrmions[1-6] emerge as promising candidates for information carriers in high-density memory[7-9], neuromorphic computing applications[10] and logic components[11] due to their unusual topological properties and emergent electromagnetic phenomenon[12,13]. Although the stability of both skyrmions and antiskyrmions is predominantly determined by the Dzyaloshinskii–Moriya interaction (DMI) in competition with other magnetic interactions[1,14], the stringent requirements of anisotropic DMI and four-fold rotoinversion symmetry for antiskyrmions make the hosting magnets fairly rare[4,15,16]. Skyrmions stabilized by DMI have been extensively studied in both bulk and thin-film systems, and even their current-induced movement controlled by spin-transfer torque (STT) or spin–orbit torque has been theoretically and experimentally

demonstrated in a ferromagnetic background[7,17,18]. Theoretically, skyrmions can alternatively be stabilized within a helical background, where they might exhibit higher mobility because of being confined in the helical stripes but pending experimental validation[19]. The antiskyrmion structure is composed of intricate chiral boundaries that alternates between helical (Bloch-type) and cycloidal (Néel-type) spin patterns[5,20], with a topological charge of $Q = \pm 1$, defined by

$$Q = (1/4\pi) \iint \mathbf{n} \cdot \left(\frac{\partial \mathbf{n}}{\partial x} \times \frac{\partial \mathbf{n}}{\partial y} \right) \mathrm{d}x\mathrm{d}y \quad \text{(ref. 12)}.$$ The experimental progress on revealing the antiskyrmion dynamic properties proceeds very slowly despite the advantage of a wider temperature range[5,21].

The current-driven antiskyrmion behaviour has been theoretically proposed on the basis of the STT model[22], similar to skyrmions, and

[1]Beijing National Laboratory for Condensed Matter Physics, Institute of Physics, Chinese Academy of Sciences, Beijing, China. [2]School of Physical Sciences, University of Chinese Academy of Sciences, Beijing, China. [3]State Key Laboratory for Mesoscopic Physics and Frontiers Science Center for Nano-optoelectronics, School of Physics, Peking University, Beijing, China. [4]Department of Energy and Power Engineering, School of Mechanical Engineering, Beijing Institute of Technology, Beijing, China. [5]Anhui Key Laboratory of Magnetic Functional Materials and Devices, School of Materials Science and Engineering, Anhui University, Hefei, China. [6]Key Laboratory of Advanced Materials, School of Materials Science and Engineering, Tsinghua University, Beijing, China. [7]Theoretical Division and Center for Integrated Nanotechnologies, Los Alamos National Laboratory, Los Alamos, NM, USA. [8]Songshan Lake Materials Laboratory, Dongguan, China. [9]Ningbo Institute of Materials Technology & Engineering, Chinese Academy of Sciences, Ningbo, China. ✉e-mail: szl@lanl.gov; zhangy@iphy.ac.cn
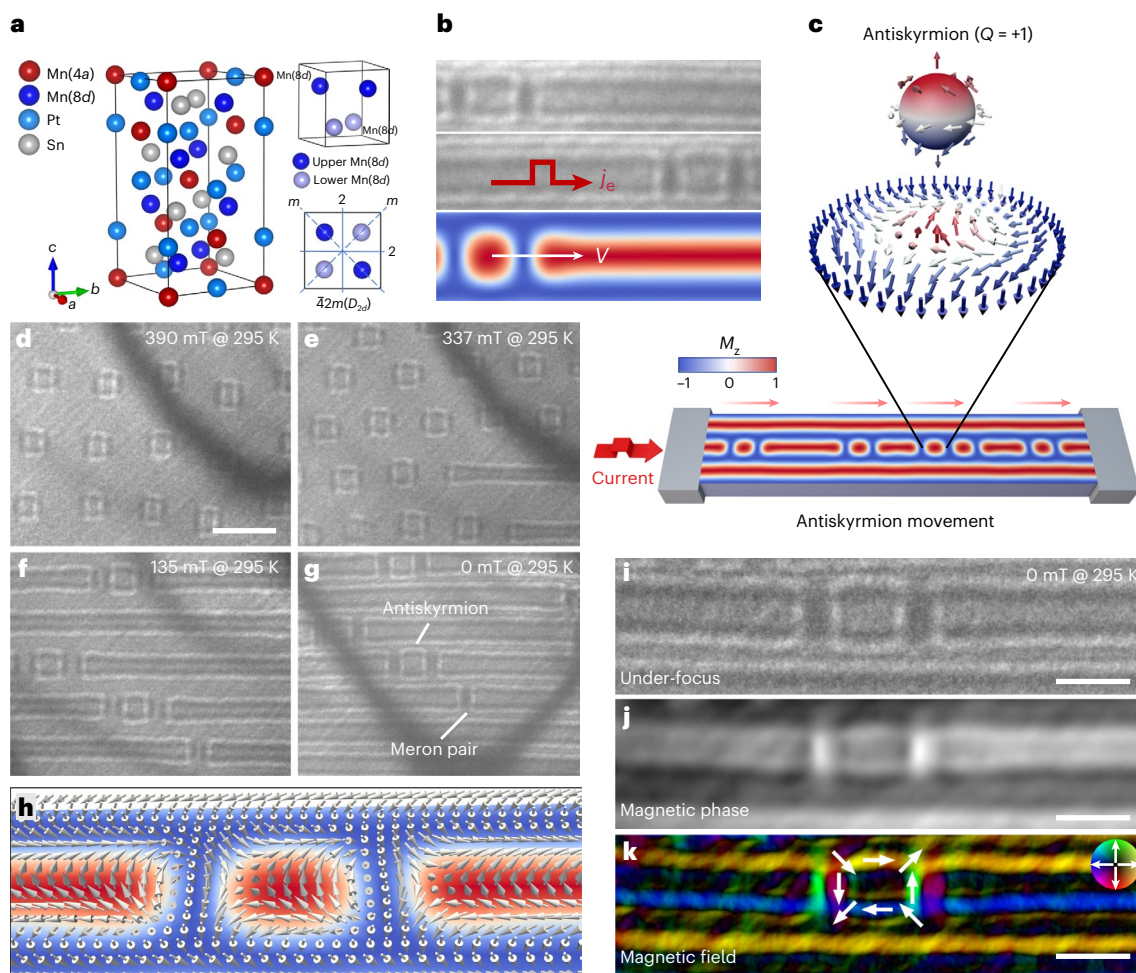
Fig. 1 | Realization of room-temperature antiskyrmions with different magnetization states and their straight current-driven behaviour along the naturally helical stripes at zero field in a Mn$_{1.4}$PtSn chiral magnet.
a, Schematic of the Mn$_{1.4}$PtSn crystal structure with overall D_{2d} symmetry and I_4m_2 symmetry along the [001] direction. **b**, Current-driven antiskyrmion movement along a straight helical stripe at zero field. **c**, Schematic of a scenario involving antiskyrmions moving along a natural track under an electric current. **d**–**g**, L-TEM images showing the representative different antiskyrmion states

from the antiskyrmion lattice in a ferromagnetic background to the isolated antiskyrmion in helical stripes while decreasing the magnetic field to zero. **h**, Simulation snapshot of an antiskyrmion in the stripe domain showing the spin configuration. **i**, Enlarged under-focus Fresnel L-TEM image of the zero-field antiskyrmion in the helical stripe. **j**,**k**, Corresponding real-space magnetic phase (**j**) and spin configuration (**k**) deduced from the TIE. The arrows and colour scale indicate the direction and magnitude of the in-plane magnetization. Scale bar, 100 nm.

the electric-current-induced Magnus force often results in undesired lateral deflection and eventual annihilation at the sample edges, which is known as the skyrmion Hall effect[23,24]. However, the experimental demonstration of antiskyrmion motion has not been achieved yet. This could be due to the specific broken rotational symmetry and emergent quadrupolar moment of magnetostatic charge[4,25] in antiskyrmions, giving rise to intricate antiskyrmion interactions and unknown obstacles within the typical ferromagnetic background phase[26,27]. Therefore, to advance both fundamental research and application, it is essential to experimentally demonstrate the movement of antiskyrmions via electric current to address the critical gap in current literature.

In this study, we successfully demonstrate the current-driven dynamics of antiskyrmions in a Mn$_{1.4}$PtSn chiral magnet at room temperature and without any magnetic field using dedicated Lorentz transmission electron microscopy (L-TEM). In contrast to the common manipulation of topological skyrmions in the ferromagnetic background, which hinders the motion of antiskyrmions, we experimentally confine antiskyrmions within strong-correlated helical stripe channels, along which antiskyrmion sliding is launched under a low current density. Furthermore, the specific DMI-vector-determined spin spiral domains with D_{2d} symmetry provide naturally straight channels to

confine the antiskyrmion movement without deflection. The higher mobility of the antiskyrmions in helical stripe domains in contrast to a typical ferromagnetic background is well understood via micromagnetic simulations and collective pinning theory, which could be applicable to other topological spin textures.

Realization of zero-field antiskyrmion sliding in stripe domains

The existence of antiskyrmions in single-crystal Mn$_{1.4}$PtSn[5,28] is determined by its acentric tetragonal space group I_4m_2 with D_{2d} symmetry (Fig. 1a shows the schematic), which allows for the anisotropic DMI vector fields with opposite signs in the x and y directions. Here the DMI energy can be written as $E_{DMI} = Dd \iint (\pm L_{yz}^{(x)} - L_{zx}^{(y)}) \, dxdy$, where D is the DMI strength, d is the film thickness and $L_{zx}^{(y)} = n_z \frac{\partial n_x}{\partial y} - n_x \frac{\partial n_z}{\partial y}$ and $L_{yz}^{(x)} = n_y \frac{\partial n_z}{\partial x} - n_z \frac{\partial n_y}{\partial x}$ represent Lifshitz invariants with the unit vector $\mathbf{n} = (n_x, n_y, n_z)$ for the magnetization direction. The anisotropic DMI results in the ground state of naturally straight stripe domains with screw spin modulation at zero field, where the helical propagation wavevectors are fixed along the [010] and [100] directions
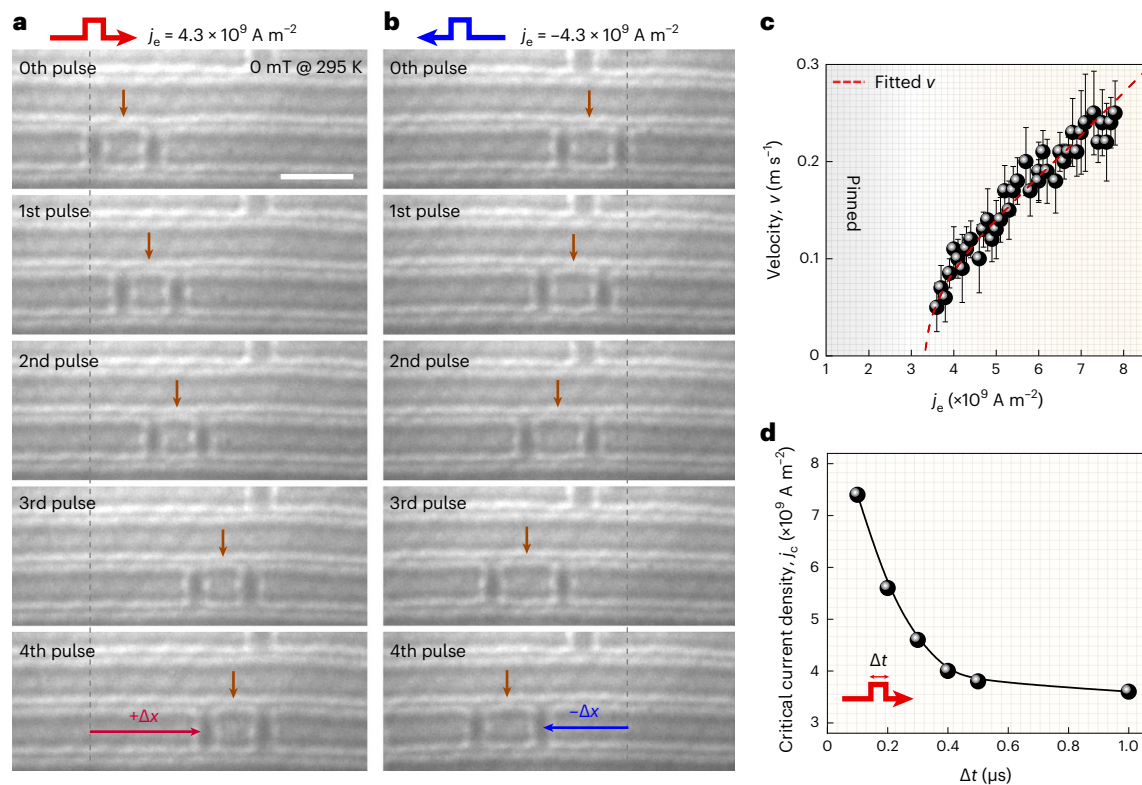
Fig. 2 | Room-temperature antiskyrmion sliding along the straight stripe domain at a current density of $j_e = 4.3 \times 10^9$ A m^{-2} but with two opposite directions at zero field. a, L-TEM images showing the trajectory of antiskyrmion along the x axis under a series of positive electric current pulses. Scale bar, 200 nm. **b**, Opposite antiskyrmion movement when the pulse current is reversed to the opposite direction. The arrows mark the antiskyrmion position relative to the initial position with dotted lines. The consistent directions for electric current and antiskyrmion trajectory are indicated on the corresponding images. **c**, Dependence of the averaged velocities of the antiskyrmion on the current density, with linear fitting to the standard depinning theory, namely, $v \approx \sqrt{j_e - j_c}$. The error bars represent the standard deviation based on 30 measurements. **d**, Dependence of critical current density j_c on the pulse width when driving the antiskyrmion movement along the helical stripe.

(Supplementary Fig. 1)[5,29]. The antiskyrmions maintain good thermal stability up to the Curie temperature of nearly 400 K, which gives the advantage of antiskyrmion manipulation near room temperature.

We fabricate a thin Mn$_{1.4}$PtSn microdevice with Pt electrodes on both sides of the sample by using a focused-ion beam (Methods and Supplementary Fig. 2). We then focus on the L-TEM imaging of a single antiskyrmion along a straight stripe domain in the presence of electric current pulses, where the experimental evidence of the antiskyrmion sliding movement is observed at a current density of $j_e = 4.3 \times 10^9$ A m^{-2} at zero magnetic field (Fig. 1b). The schematic of a scenario involving antiskyrmions moving along a natural track (Fig. 1c) illustrates that these topological structures could be used as information carriers in devices similar to racetrack memory. The spin spiral period and corresponding antiskyrmion diameter are measured to be approximately 140 nm. The antiskyrmion is embedded into a stripe domain, which enables strong magnetization correlation as a composite object. Following the movement of the antiskyrmion, the stripe domain behind (ahead) the antiskyrmion accordingly stretches (shrinks) through local magnetization rotation. The critical contribution of the stripe domain towards initiating antiskyrmion movement is demonstrated by comparing with the common ferromagnetic background. Antiskyrmions in the typical ferromagnetic background at a magnetic field of about 390 mT (Fig. 1d) are extremely difficult to move even at a higher electric current density of $j_e = 4.0 \times 10^{10}$ A m^{-2} (Supplementary Fig. 3).

We have developed a reliable and reproducible experimental protocol to create a single antiskyrmion in the helical phase at zero field. By decreasing the magnetic field, an isolated antiskyrmion and meron pair within the stripe domains could be obtained while going through

the phase transition from the antiskyrmion lattice to the helical phase (Fig. 1d–g) (Supplementary Fig. 4 provides further details). Further investigation of the antiskyrmion nucleation at a specific location of the stripe in a suitable thin film could enhance the compatibility of using antiskyrmions as information bits in spintronics. By analysing the L-TEM images (Supplementary Fig. 5) at under-focused Fresnel modes ($\Delta z = 250$ μm) (Fig. 1i) and using the transport-of-intensity equation (TIE) method[30] to visualize the in-plane magnetization distribution of magnetic phase (Fig. 1j) and corresponding spin texture (Fig. 1k), the spin configuration of the antiskyrmion is identified, consistent with previous studies[20,31]. The simulated L-TEM images and magnetic phase (Supplementary Fig. 6) further confirm the antiskyrmion spin configuration.

To better understand the experimental results, we perform a series of simulations with the periodic (open) boundary condition along the x (y) direction by using the parameters extracted from the magnetic property measurements (Supplementary Fig. 7). The spin configuration of an antiskyrmion in the helical stripe domain (Fig. 1h) is consistent with the experimental image (Fig. 1k) and the current-driven antiskyrmion movement within the helical stripe is reproduced in simulations (Fig. 1b). It is worth noting that the strongly correlated spin system can be treated as a continuum-ordered spiral medium with localized spin dislocation on both sides of the antiskyrmion, analogous to dislocation defects[32–34] in crystalline materials or cholesteric liquid crystals[35,36]. The unique features of driving (anti)skyrmions in the helical stripes including straight movement without deflection under a low current density and good stability in a wide temperature range and zero field are beneficial to spintronic applications (Supplementary Note I).
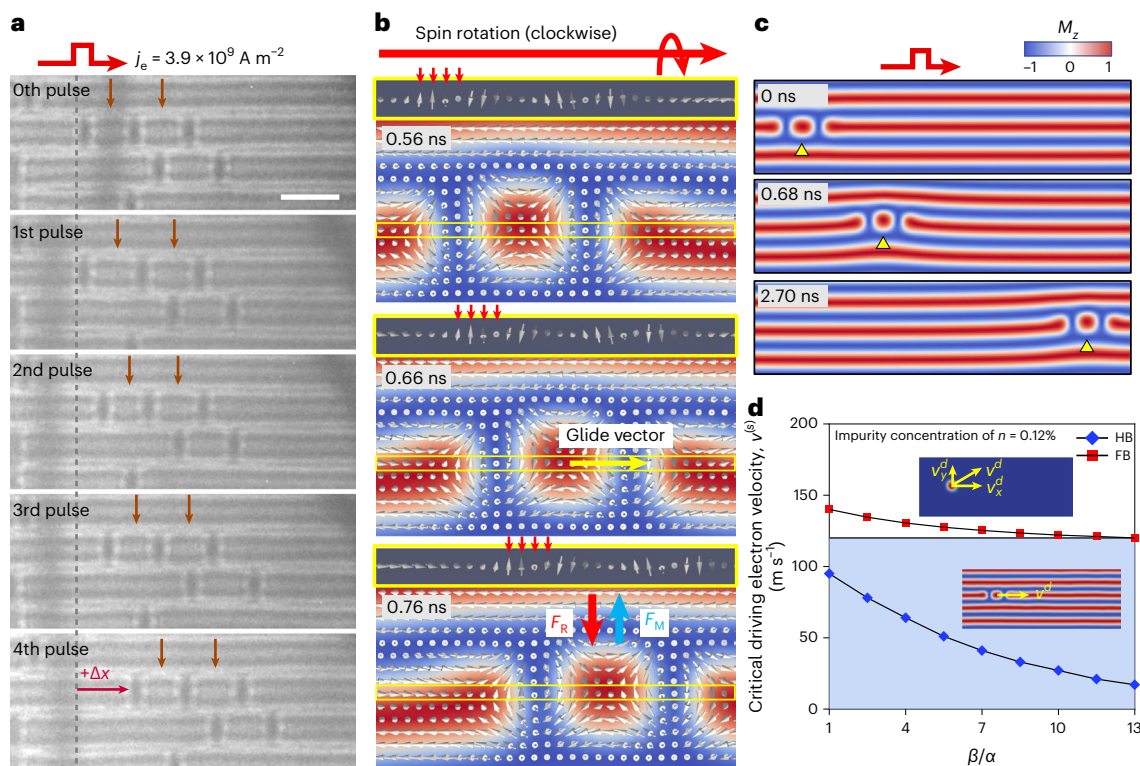
Fig. 3 | Collective sliding of antiskyrmion and antiskyrmion dimer ($Q = 2$) **along a straight stripe in Mn$_{1.4}$PtSn thin plate at zero field and room temperature. a**, L-TEM images for the position change of antiskyrmion dimer ($Q = 2$) along the parallel stripes after sequentially applying electric pulses at a current density of $j_e = 3.9 \times 10^9$ A m^{-2}. Scale bar, 200 nm. **b**, Enlarged spin configuration near the antiskyrmion demonstrates the precession of localized magnetic moments along the x-helical axis. F_M represents the Magnus force associated with the antiskyrmion Hall effect, and F_R represents the repulsive interaction force. **c**, Micromagnetic simulations of single antiskyrmion dynamics at the nanosecond scale. The antiskyrmion position is marked with a yellow triangle. The colour scale shows the out-of-plane magnetization component along the z direction. **d**, Simulated critical driving electron velocity $v^{(s)}$ as a function of β/α for antiskyrmion depinning in the respective helical and ferromagnetic backgrounds with an impurity concentration of $n = 0.12\%$. HB and FB represent the antiskyrmions in the helical and ferromagnetic background, respectively.

We then focus on the magnetization dynamics after the electric current pulse is applied parallel to the stripe domain in a nanodevice. It is shown that a critical pulsed current density is needed ($j_e > 3.6 \times 10^9$ A m^{-2} for a fixed pulse width (τ) of 1 μs) to launch the continuous movement of the antiskyrmion after overcoming the inherent pinning effect. The representative snapshots of enlarged antiskyrmion movement (Fig. 2a,b) are extracted from Supplementary Fig. 8. The dependence of antiskyrmion position on the number of current pulses demonstrates the controllable movement along the spiral track without any apparent lateral movement, successfully avoiding the antiskyrmion Hall effect[22] (Supplementary Video 1). The direction reversal of antiskyrmion movement on reversing the current (Fig. 2b and Supplementary Video 2) manifests the dominant contribution of current-induced STT. The average velocity v is calculated to be about 0.1 m s^{-1} at a current density of $j_e = 4.3 \times 10^9$ A m^{-2} by measuring the position of the antiskyrmion versus pulse period. The summarized relationship between the antiskyrmion velocity and current density (Fig. 2c) follows the standard depinning theory as $v \approx \sqrt{j_e - j_c}$ (ref. 37). We estimate the mobility of the antiskyrmion by the derivative $(\frac{dv}{dj_e})$ in the linear segment of Fig. 2c, where it undergoes a steady motion, and the mobility of about 4.3×10^{-11} m^3 (A s)$^{-1}$ is obtained by applying a linear fit. The mobility of antiskyrmions is comparable with that of skyrmions in chiral magnets[38–40]. The critical current density j_c is defined for initial depinning when an antiskyrmion starts to move and the dependence on pulse width is shown in Fig. 2d on the basis of the L-TEM observation. For antiskyrmion-driven movement, the current density ranges from 3.6 to 8.0 ($\times 10^9$ A m^{-2}) for a pulse width of 1 μs, which is comparable and even lower than the skyrmion movement in Ta/CoFeB/TaO$_x$ films[23,41], chiral FeGe[38] and Co–Zn–Mn magnets[40]. We show that antiskyrmions merge into stripe domains and disappear when the current density exceeds a certain threshold (Supplementary Fig. 9) and that longer pulse widths reduce the current density due to the assisted Joule heating effect[41]. By applying shorter pulse widths, we can achieve higher current densities and drive the antiskyrmions at faster speeds (Supplementary Fig. 10). The experimental demonstration of current-driven antiskyrmions along the straight stripe track opens up new possibilities for manipulating the position and speed of these topological spin textures.

Mechanism of antiskyrmion sliding in stripe domains

It is noteworthy that the antiskyrmion-dimer-bound ($Q = 2$) states or even multimer-bound states consistently demonstrate collective movement under an electric current due to the mutual interaction with the helical phase (Fig. 3a and Supplementary Fig. 11). According to the numerical simulations, we emphasize the contribution of STT[7,17,22] on launching the antiskyrmion movement. The dynamic evolution of magnetization at the nanosecond scale clearly shows the precession of localized magnetic moments on both sides of the antiskyrmion along the x axis (Fig. 3b) induced by a field-like out-of-plane torque, eventually leading to antiskyrmion sliding. The spin dynamics under the current drive can be intuitively understood in analogy with the disruption of atomic bonding near the dislocation line, where the Peierls stress is greatly lowered because of local dislocation gliding[42]. Thus,
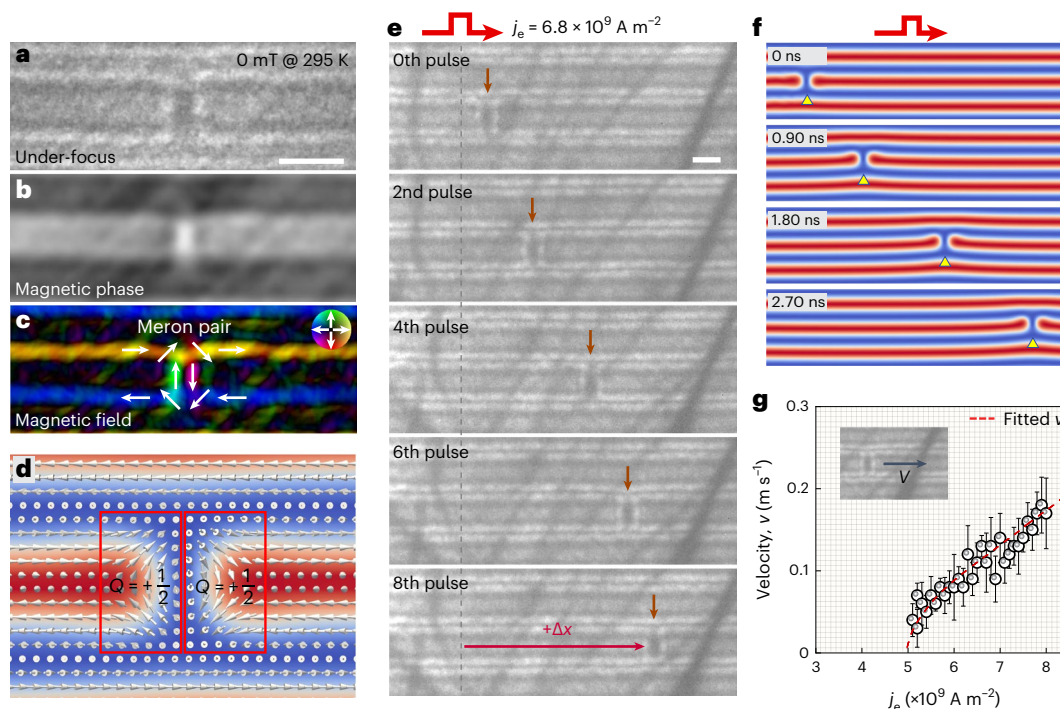
Fig. 4 | Current-driven behaviour of room-temperature meron pair along a helical stripe at zero field in Mn$_{1.4}$PtSn chiral magnet. a–d, Identification of the meron pair with a topological charge of $Q = 1/2$ for each meron in the under-focus L-TEM image, magnetic-phase image, spin texture of the meron pair from the TIE analysis and the spin configuration obtained from micromagnetic simulation. The topological charge of a single meron ($Q = 1/2$) is indicated by the solid red line box. **e**, L-TEM images of a meron pair showing position change at a pulsed current density of $j_e = 6.8 \times 10^9$ A m^{-2}. Scale bar, 100 nm. **f**, Micromagnetic simulations of the movement of a meron pair initiated by electric current at the nanosecond scale. The yellow triangle marks the position change of the meron pair. **g**, Dependence of the averaged velocity of meron pairs on the current density with linear fit to the standard depinning theory. The error bars represent the standard deviation based on 30 times measurements.

this antiskyrmion sliding via local magnetization variation could be akin to the dislocation gliding process[37–39].

To better understand the low pinning current for an antiskyrmion embedded in a stripe domain, we consider two dominant factors. First, the confinement of antiskyrmions by stripe domains can effectively increase the driving force by following different dynamic velocity equations in the respective helical and ferromagnetic background, as demonstrated via micromagnetic simulations. By assuming a rigid topological spin structure as a quasiparticle, we describe STT-induced antiskyrmion dynamics based on the Thiele equation: $\mathbf{G} \times (\mathbf{v}^{(s)} - \mathbf{v}^{(d)}) + D(\beta\mathbf{v}^{(s)} - \alpha\mathbf{v}^{(d)}) + \mathbf{F}_h = 0$ (refs. 12,13), where $v^{(d)} = (v_x^{(d)}, v_y^{(d)})$ is the antiskyrmion movement velocity and $\mathbf{v}^{(s)} = -\frac{gP\mu_B}{2eM_s}\mathbf{j} = b\mathbf{j}$ is the velocity of driving electrons, representing the action of the spin-polarized current (Supplementary Note II). The first gyrotropic term describes the Magnus force and leads to a dominant antiskyrmion Hall effect because both Gilbert damping α and non-adiabatic STT β are much smaller than 1. The current-induced lateral Magnus force deflects the antiskyrmion and nearby helical stripes in the upward direction and the corresponding repulsion from the edge of the straight stripe decreases the overall transverse displacement of the antiskyrmion (Fig. 3b,c), ultimately confining the antiskyrmion sliding along the straight stripe domain (Supplementary Fig. 12). When the confinement force $\mathbf{F}_h$ from the edge restriction of the helical stripes totally balances the topological gyrotropic term, the velocity of the antiskyrmion sliding along the helical track can be written as $v^{(d)} = \frac{\beta}{\alpha}v^{(s)}$ (refs. 7,23). This is clearly distinguished from the antiskyrmions in a ferromagnetic background, where the longitudinal and lateral velocities of the antiskyrmions follow different formulas: $v_x^{(d)} = \frac{G^2 + D^2\alpha\beta}{G^2 + \alpha^2 D^2}v^{(s)}$ and $v_y^{(d)} = \frac{(\alpha - \beta)DG}{G^2 + \alpha^2 D^2}v^{(s)}$, respectively (Supplementary Note II).

Second, on the basis of collective pinning theory, the larger scale of the rigid composite object could easily smear out the random pinning potential. The pinning effect is added by introducing easy-axis magnetic anisotropy in the system at a certain impurity concentration (Supplementary Note III). Therefore, a threshold current density is required to depin the antiskyrmion away from the local pinning potential. It is demonstrated that the critical electric current for antiskyrmion depinning from a helical stripe is much smaller than that from the ferromagnetic background at the same impurity concentration, that is, $n = 0.12\%$ (Fig. 3d), especially at higher β/α values, where the Gilbert damping α is fixed at a typical value of 0.05 for ferromagnetic metals and the non-adiabatic coefficient β value varies from 0.05 to 0.65. The dependence of critical driving electron velocity $v^{(s)}$ on the increased β/α value for helical stripe (HB) and ferromagnetic background (FB) (Fig. 3d) corresponds well with the above dynamic formula equations. Moreover, the rigid composite object of an antiskyrmion embedded in a stripe domain decreases the pinning potential by averaging over the disorder potential[43] (Supplementary Note III). However, for a single antiskyrmion in the ferromagnetic background, the antiskyrmion can be individually pinned by the defect and thus the pinning is strong. The simulation results are consistent with the prior theoretical expectation that helical stripes create natural lanes for fast skyrmion motion[19].

Meron sliding in stripe domains at zero field

The topological spin texture of the meron pair with half-integer topological charge[44–47] is further identified by under-focus L-TEM images (Supplementary Fig. 13). The obvious position shift of the meron pair along the straight track (Supplementary Video 3) under an electric current density of 6.8×10^9 A m^{-2} (Fig. 4e) at zero field and room temperature verifies the effectiveness of the topological texture sliding

mechanism. Under a series of current pulses, the topology of the meron pair remains intact with only localized magnetization rotating to the appropriate direction, which is further confirmed by a corresponding micromagnetic simulation (Fig. 4f). Interestingly, the dynamic simulations also reveal negligible lateral deflection due to the balance between the skyrmion Hall effect[48] and the repulsion from the helical stripe boundary, similar to the above analysis for antiskyrmions. The relationship between current density and meron velocity (Fig. 4g) indicates a slightly lower velocity at a given electric current and higher depinning current density compared with those of the antiskyrmion. This difference in velocity and threshold current can be attributed to the topological differences between the antiskyrmion and meron pair[49].

Conclusion

In this study, we have experimentally demonstrated the current-driven dynamics of antiskyrmions in a $Mn_{1.4}PtSn$ chiral magnet at room temperature, without the need for an external magnetic field. By confining antiskyrmions within helical stripe domains as a composite object, we have successfully launched and controlled their sliding movement along one-dimensional tracks with low current density, overcoming the challenges from pinning and lateral deflection for antiskyrmions in a typical ferromagnetic background. The dominant factors for the higher mobility of antiskyrmions embedded in helical stripes are discussed, manifesting the contribution of increased driving force and averaged pinning potential as unravelled by micromagnetic simulation and the collective pinning theory. We further show that our method can be applied to the sliding motion of merons in stripe domains. Our findings provide a clear demonstration and comprehensive understanding of antiskyrmion gliding along straight stripe tracks under a low current density.

Online content

Any methods, additional references, Nature Portfolio reporting summaries, source data, extended data, supplementary information, acknowledgements, peer review information; details of author contributions and competing interests; and statements of data and code availability are available at https://doi.org/10.1038/s41563-024-01870-8.

References

1. Bogdanov, A. N. & Yablonskii, D. Thermodynamically stable 'vortices' in magnetically ordered crystals. The mixed state of magnets. *Zh. Eksp. Teor. Fiz.* **95**, 178–182 (1989).
2. Mühlbauer, S. et al. Skyrmion lattice in a chiral magnet. *Science* **323**, 915–919 (2009).
3. Yu, X. et al. Real-space observation of a two-dimensional skyrmion crystal. *Nature* **465**, 901–904 (2010).
4. Koshibae, W. & Nagaosa, N. Theory of antiskyrmions in magnets. *Nat. Commun.* **7**, 10542 (2016).
5. Nayak, A. K. et al. Magnetic antiskyrmions above room temperature in tetragonal Heusler materials. *Nature* **548**, 561–566 (2017).
6. Fert, A., Reyren, N. & Cros, V. Magnetic skyrmions: advances in physics and potential applications. *Nat. Rev. Mater.* **2**, 17031 (2017).
7. Iwasaki, J., Mochizuki, M. & Nagaosa, N. Current-induced skyrmion dynamics in constricted geometries. *Nat. Nanotechnol.* **8**, 742–747 (2013).
8. Tomasello, R. et al. A strategy for the design of skyrmion racetrack memories. *Sci. Rep.* **4**, 6784 (2014).
9. Parkin, S. & Yang, S.-H. Memory on the racetrack. *Nat. Nanotechnol.* **10**, 195–198 (2015).
10. Grollier, J. et al. Neuromorphic spintronics. *Nat. Electron.* **3**, 360–370 (2020).
11. Zhou, Y. Magnetic skyrmions: intriguing physics and new spintronic device concepts. *Natl Sci. Rev.* **6**, 210–212 (2019).
12. Nagaosa, N. & Tokura, Y. Topological properties and dynamics of magnetic skyrmions. *Nat. Nanotechnol.* **8**, 899–911 (2013).
13. Schulz, T. et al. Emergent electrodynamics of skyrmions in a chiral magnet. *Nat. Phys.* **8**, 301–304 (2012).
14. Leonov, A. et al. The properties of isolated chiral skyrmions in thin magnetic films. *New J. Phys.* **18**, 065003 (2016).
15. Hoffmann, M. et al. Antiskyrmions stabilized at interfaces by anisotropic Dzyaloshinskii–Moriya interactions. *Nat. Commun.* **8**, 308 (2017).
16. Kovalev, A. A. & Sandhoefner, S. Skyrmions and antiskyrmions in quasi-two-dimensional magnets. *Front. Phys.* **6**, 98 (2018).
17. Sampaio, J., Cros, V., Rohart, S., Thiaville, A. & Fert, A. Nucleation, stability and current-induced motion of isolated magnetic skyrmions in nanostructures. *Nat. Nanotechnol.* **8**, 839–844 (2013).
18. Jiang, W. et al. Blowing magnetic skyrmion bubbles. *Science* **349**, 283–286 (2015).
19. Müller, J. et al. Magnetic skyrmions and skyrmion clusters in the helical phase of Cu_2OSeO_3. *Phys. Rev. Lett.* **119**, 137201 (2017).
20. Karube, K. et al. Room-temperature antiskyrmions and sawtooth surface textures in a non-centrosymmetric magnet with S_4 symmetry. *Nat. Mater.* **20**, 335–340 (2021).
21. Saha, R. et al. Intrinsic stability of magnetic anti-skyrmions in the tetragonal inverse Heusler compound $Mn_{1.4}Pt_{0.9}Pd_{0.1}Sn$. *Nat. Commun.* **10**, 5305 (2019).
22. Huang, S. et al. Stabilization and current-induced motion of antiskyrmion in the presence of anisotropic Dzyaloshinskii–Moriya interaction. *Phys. Rev. B* **96**, 144412 (2017).
23. Jiang, W. et al. Direct observation of the skyrmion Hall effect. *Nat. Phys.* **13**, 162–169 (2016).
24. Litzius, K. et al. Skyrmion Hall effect revealed by direct time-resolved X-ray microscopy. *Nat. Phys.* **13**, 170–175 (2017).
25. He, Z. et al. Visualizing emergent magnetic flux of antiskyrmions in $Mn_{1.4}PtSn$ magnet. *Adv. Funct. Mater.* **32**, 2112661 (2022).
26. Zhang, X. et al. Skyrmion-skyrmion and skyrmion-edge repulsions in skyrmion-based racetrack memory. *Sci. Rep.* **5**, 7643 (2015).
27. Reichhardt, C. & Reichhardt, C. O. Depinning and nonequilibrium dynamic phases of particle assemblies driven over random and ordered substrates: a review. *Rep. Prog. Phys.* **80**, 026501 (2016).
28. Vir, P. et al. Tetragonal superstructure of the antiskyrmion hosting Heusler compound $Mn_{1.4}PtSn$. *Chem. Mater.* **31**, 5876–5880 (2019).
29. Ma, T. et al. Tunable magnetic antiskyrmion size and helical period from nanometers to micrometers in a D_{2d} Heusler compound. *Adv. Mater.* **32**, 2002043 (2020).
30. Ishizuka, K. & Allman, B. Phase measurement of atomic resolution image using transport of intensity equation. *J. Electron Microsc.* **54**, 191–197 (2005).
31. Peng, L. et al. Controlled transformation of skyrmions and antiskyrmions in a non-centrosymmetric magnet. *Nat. Nanotechnol.* **15**, 181–186 (2020).
32. Hirsch, P., Horne, R. & Whelan, M. Direct observations of the arrangement and motion of dislocations in aluminium. *Philos. Mag.* **1**, 677–684 (1956).
33. Anderson, P. M., Hirth, J. P. & Lothe, J. *Theory of Dislocations* (Cambridge Univ. Press, 2017).
34. Schoenherr, P. et al. Topological domain walls in helimagnets. *Nat. Phys.* **14**, 465–468 (2018).
35. Chuang, I., Durrer, R., Turok, N. & Yurke, B. Cosmology in the laboratory: defect dynamics in liquid crystals. *Science* **251**, 1336–1342 (1991).
36. Zapotocky, M., Ramos, L., Poulin, P., Lubensky, T. & Weitz, D. Particle-stabilized defect gel in cholesteric liquid crystals. *Science* **283**, 209–212 (1999).

37. Brazovskii, S. & Nattermann, T. Pinning and sliding of driven elastic systems: from domain walls to charge density waves. *Adv. Phys.* **53**, 177–252 (2004).

38. Tang, J. et al. Magnetic skyrmion bundles and their current-driven dynamics. *Nat. Nanotechnol.* **16**, 1086–1091 (2021).

39. Wang, W. et al. Electrical manipulation of skyrmions in a chiral magnet. *Nat. Commun.* **13**, 1593 (2022).

40. Peng, L. et al. Dynamic transition of current-driven single-skyrmion motion in a room-temperature chiral-lattice magnet. *Nat. Commun.* **12**, 6797 (2021).

41. Yu, G. et al. Room-temperature skyrmion shift device for memory application. *Nano Lett.* **17**, 261–268 (2017).

42. Nabarro, F. Fifty-year study of the Peierls–Nabarro stress. *Mater. Sci. Eng. A* **234**, 67–76 (1997).

43. Blatter, G., Feigel'man, M. V., Geshkenbein, V. B., Larkin, A. I. & Vinokur, V. M. Vortices in high-temperature superconductors. *Rev. Mod. Phys.* **66**, 1125 (1994).

44. Ezawa, M. Compact merons and skyrmions in thin chiral magnetic films. *Phys. Rev. B* **83**, 104416 (2011).

45. Lin, S.-Z., Saxena, A. & Batista, C. D. Skyrmion fractionalization and merons in chiral magnets with easy-plane anisotropy. *Phys. Rev. B* **91**, 224407 (2015).

46. Yu, X. et al. Transformation between meron and skyrmion topological spin textures in a chiral magnet. *Nature* **564**, 95–98 (2018).

47. Jani, H. et al. Antiferromagnetic half-skyrmions and bimerons at room temperature. *Nature* **590**, 74–79 (2021).

48. Hirata, Y. et al. Vanishing skyrmion Hall effect at the angular momentum compensation temperature of a ferrimagnet. *Nat. Nanotechnol.* **14**, 232–236 (2019).

49. Iwasaki, J., Mochizuki, M. & Nagaosa, N. Universal current-velocity relation of skyrmion motion in chiral magnets. *Nat. Commun.* **4**, 1463 (2013).

Methods

Preparation of Mn$_{1.4}$PtSn single crystals

Mn$_{1.4}$PtSn single crystals were grown using the flux growth method with Sn as the flux[5,28]. Highly purified Mn (99.999%) and Pt (99.999%) metals in a 3:1 M (molar) ratio with a total weight of 0.75 g plus approximately 10.00 g Sn were loaded into an alumina crucible. Subsequently, the alumina crucible was sealed in a quartz tube at 0.2 bar argon pressure and then heated in a box furnace for 24 h at 1,323 K to achieve a homogeneous composition. After that, it was rapidly cooled to 923 K and then slowly cooled to and maintained at 723 K for 48 h for better crystallization before removing the extra flux by centrifugation.

Fabrication of Mn$_{1.4}$PtSn microdevices

A Mn$_{1.4}$PtSn thin plate with a thickness of approximately 150 nm for real-space L-TEM observation was fabricated on an electric chip by using the lift-out method in a focused-ion-beam microscope (ZEISS 550 focused-ion beam) where a gas injection system and a micromanipulator (MM3A, Kleindiek) are included. The two ends of the thin plate with Pt electrodes are connected to a voltage source and the orientation of the Mn$_{1.4}$PtSn thin plate was identified via a selected-area diffraction pattern. Supplementary Fig. 2 shows further details regarding the setup of in situ electric Mn$_{1.4}$PtSn microdevices for transmission electron microscopy manipulation.

Magnetic-domain imaging and manipulation in L-TEM

The real-space magnetic-domain imaging was carried out using the Lorentz Fresnel method in a dedicated JEOL L-TEM instrument (JEOL2100F) operated at 200 kV. The observed magnetic-domain contrast can be qualitatively understood on the basis of the interaction of the electron beam with the in-plane magnetization, introducing the Lorentz force to deflect the high-voltage electrons as they pass through the magnetic sample. Magnetic-domain wall contrast is imaged at the respective defocus and over-focus states by a charge-coupled device camera. Subsequently, the magnetic-phase images are extracted and high-resolution in-plane magnetization maps are obtained via a TIE analysis[30] (main text and Supplementary Figs. 5 and 13). Antiskyrmion manipulation as a response of the electric current is performed using a double-tilt electric transmission electron microscopy holder (DENSsolutions) with a d.c. pulsed electric current provided via a source instrument (Keithley 2601B).

Characterization of magnetization textures

L-TEM represents a powerful tool for elucidating the magnetization configurations in magnetic samples. This capability arises from the inherent interaction between incident electrons and the in-plane magnetization of the specimen. Consequently, when examining the in-plane magnetization intensity distribution in the defocused L-TEM image, the convergence (divergence) of the electron beam results in the manifestation of contrasting features. Specifically, bright (dark) contrast becomes evident in the image, depending on the defocus condition. This contrast polarity inversely varies between the under-focused and over-focused L-TEM images when maintained at the same defocus setting. The analysis of the magnetized texture is based on the TIE[30]:

$$\frac{2\pi}{\lambda}\frac{\partial I(x,y,z)}{\partial z} = -\nabla_{\mathbf{xy}}(I(x,y,z)\nabla_{\mathbf{xy}}\Phi(x,y,z)), \qquad (1)$$

$$\nabla_{\mathbf{xy}}\Phi(x,y,z) = -\frac{e}{\hbar}(\mathbf{M}\times\mathbf{n})t. \qquad (2)$$

The first equation elucidates the connection between the intensity denoted as $I(x,y,z)$ and the phase represented as $\Phi(x,y,z)$, with λ denoting the spectrally weighted mean wavelength of the illumination. The TIE analysis was conducted on the basis of three recorded Lorentz Fresnel images in the under-focus, in-focus and over-focus conditions. Image alignment was manually conducted first to correct the image rotation and change in magnification at a variable defocus value. QPt software was used to retrieve the phase images. By using the second equation, the projected in-plane magnetization distribution was obtained by calculating the gradient of the phase. Also, $\mathbf{n}$ is the unit vector along the beam direction, $\mathbf{M}$ is the magnetization vector and t is the sample thickness.

Micromagnetic simulations

We incorporated anisotropic DMI and improved the numerical precision to personalize the code on the basis of the well-established GPU-accelerated programme MuMax[50]. The energy functional is given by

$$E = \int_{V_s} (\varepsilon_{ex} + \varepsilon_{dmi} + \varepsilon_a + \varepsilon_{Zeeman} + \varepsilon_{dem})d\mathbf{r}, \qquad (3)$$

where the exchange interaction is $\varepsilon_{ex} = A_{ex}((\partial_x\mathbf{m})^2 + (\partial_y\mathbf{m})^2 + (\partial_z\mathbf{m})^2)$, anisotropic DMI interaction energy is $\varepsilon_{dmi} = D_{dmi}(m_z\frac{\partial m_x}{\partial x} - m_x\frac{\partial m_z}{\partial x} - m_z\frac{\partial m_y}{\partial y} + m_y\frac{\partial m_z}{\partial y})$, uniaxial anisotropy energy is $\varepsilon_a = -K_u(\mathbf{u}\cdot\mathbf{m})^2$, Zeeman energy is $\varepsilon_{Zeeman} = -M_s\mathbf{H}_{ext}\cdot\mathbf{m}$ with the external magnetic field $\mathbf{H}_{ext}$ and demagnetization energy is $\varepsilon_d = -\frac{1}{2}M_s\mathbf{H}_d\cdot\mathbf{m}$ with demagnetization field $\mathbf{H}_d$. Also, $\mathbf{m} = \mathbf{m}(\mathbf{r})$ is a unit-vector field defining the direction of magnetization $\mathbf{M} = \mathbf{m}(\mathbf{r})M_s$. Furthermore, A_{ex}, D_{dmi}, K_u and M_s are the exchange interaction, anisotropic DMI interaction, uniaxial anisotropy and saturation magnetization, respectively. The anisotropic DMI originates from the D_{2d} symmetry of the tetragonal Heusler crystals. The simulation is conducted on the basis of the experimentally measured uniaxial anisotropy $K_u = 125$ kJ m^{-3} and saturation magnetization $M_s = 637$ kA m^{-1} at $T = 300$ K (Supplementary Fig. 7). The uniaxial anisotropy K_u is extracted from the area between the $M–H$ curves along the [001] and [100] directions according to the formula $K_u = \int_0^{M_s}[H_{[001]}(M) - H_{[100]}(M)]dM$. It should be mentioned that the parameters for exchange interaction, namely, $A_{ex} = 83$ pJ m^{-1} and anisotropic DMI $D_{dmi} = 8.7$ mJ m^{-2}, are slightly adjusted from a similar simulation[5] to ensure the stabilization of the antiskyrmion, which are not limited to one specific material. The system size for the simulation is set to be 1.5 μm × 0.5 μm × 0.1 μm and discretized into a 300 × 100 × 20 cube with the periodic (open)-boundary condition along the x (y) direction. The antiskyrmion is initially positioned at the centre of the track. A direct energy minimization solver ('minimization') based on the conjugate gradient method is used to stabilize the spin textures. The current-driven magnetization dynamics are studied within the extended Landau–Lifshitz–Gilbert equation by including both adiabatic and non-adiabatic STTs (Zhang–Li model)[7,17,51] (Supplementary Note II).

Simulation of magnetic-phase shift

The interaction of incident electrons with the in-plane magnetization of the magnetic sample introduces the magnetic-phase variation, which can be calculated using

$$\phi(x,y) = \frac{2\pi e}{h}\int_{-\infty}^{+\infty} A_z(x,y,z)dz. \qquad (4)$$

In this expression, $A_z(x,y,z)$ represents the z component of the magnetic-vector potential, where z is aligned with the direction of the incident electron beam; e denotes the elementary unit of charge; and h is Planck's constant. The spin configurations were derived from micromagnetic simulations. Thereafter, the magnetic-phase images were computed using a self-customized Python code.

Simulation of L-TEM images

The wave function of the electron beam, under the phase-object approximation, is expressed by

$$\Psi_0(x,y) \propto \exp(i\phi(x,y)), \qquad (5)$$

where $\varphi(x, y)$ represents the magnetic-phase shift. At the Fresnel L-TEM mode, the wave function of the electron beam at the detector plane is given by

$$\Psi_{\Delta z}(x, y) \propto \iint dx' dy' \Psi_0(x, y) K(x - x', y - y'). \tag{6}$$

Here the kernel $K(\xi, \eta)$ function follows $K(\xi, \eta) = \exp(\frac{i\pi}{\lambda \Delta z}(\xi^2 + \eta^2))$, where λ represents the relativistic electron wavelength, defined as $\lambda = \frac{hc}{\sqrt{(eU)^2 + 2eUm_e c^2}}$. In this equation, U is the accelerating voltage constant, m_e is the electron rest mass, Δz is the defocus step and c is the speed of light. Here the parameters with an acceleration voltage U of 200 kV, sample thickness t of 100 nm and defocus step Δz of ± 250 μm are used in the simulation. All the aberrations of the microscope are set to zero. The intensity of the L-TEM image is determined by performing an inverse Fourier transform as

$$I(x, y) \propto |\Psi_{\Delta z}(x, y)|^2. \tag{7}$$

Consequently, the L-TEM images for magnetic domains are accordingly simulated (Supplementary Fig. 6).

Data availability
The data that support the findings of this study are available within the Article and its Supplementary Information. Any other relevant data are available from the corresponding authors upon reasonable request.

References
50. Vansteenkiste, A. et al. The design and verification of MuMax3. *AIP Adv.* **4**, 107133 (2014).
51. Zhang, S. & Li, Z. Roles of nonequilibrium conduction electrons on the magnetization dynamics of ferromagnets. *Phys. Rev. Lett.* **93**, 127204 (2004).

Acknowledgements

Author contributions
Y.Z. and B.S. supervised the project. Z.H., Z.C. and Z.W. synthesized the $Mn_{1.4}PtSn$ bulk crystals. Z.H. and Y.Z. performed the L-TEM observation. Z.H., Z.L. and S.-Z.L. performed the micromagnetic simulation. Z.H., S.-Z.L., J.C. and Y.Z. analysed the experimental data and plotted the figures. Z.H., S.-Z.L. and Y.Z. wrote the manuscript after discussing the data with J.S., S.W., C.S., T.Z., J.C. and B.S.

Competing interests
The authors declare no competing interests.

Additional information